Molecular Catalysis 451 (2018) 247–254

Contents lists available at ScienceDirect

Molecular Catalysis

journal homepage: www.elsevier.com/locate/mcat

# Ceria-samarium binary metal oxides: A comparative approach towards structural properties and soot oxidation activity

Anjana P Anantharaman[a], Geethu J[a], Mohammed Rishab P[a], Hari Prasad Dasari[a,*], Jong-Ho Lee[b,**], Harshini Dasari[c], G Uday Bhaskar Babu[d]

[a] Chemical Engineering Department, National Institute of Technology Karnataka, Mangalore 575025, India
[b] High-Temperature Energy Materials Research Center, Korea Institute of Science and Technology, Hwarangno 14-gil 5, Seongbuk-gu, Seoul 136-791, South Korea
[c] Chemical Engineering Department, Manipal Institute Technology, Manipal Academy of Higher Education (MAHE), Manipal 576104, India
[d] Chemical Engineering Department, National Institute of Technology Warangal, Warangal 506004, India

ARTICLE INFO

*Keywords:*
Ceria-samarium
Solid solution
Bi-phase
Band gap energy
Fluorite structure
Soot oxidation

ABSTRACT

Binary metal oxides of $CeO_2$-$Sm_2O_3$ (CS*x*, *x* varies from 10 to 90 mol%) along with pure $CeO_2$ and $Sm_2O_3$ were synthesised successfully by the EDTA-Citrate method. From XRD, Raman spectroscopy and UV–vis DRS results, the whole composition of metal oxides exist in three phases: (fluorite phase (F) (CS10-CS30), bi-phase (fluorite (F) + cubic (C)) (CS30-CS90) and cubic phase (C) ($Sm_2O_3$)). For CS*x* samples, the calculated band gap energy values obtained from the UV–vis DRS results were in between 3.0–5.1 eV and fluorite phase samples (CS10–CS30) displayed lower band gap energy values (3.04–3.07 eV) than compared to the samples in other phases. Similarly, from XPS analysis, fluorite phase samples (CS10–CS30) showed higher surface oxygen vacancy concentration than compared to samples in other phases. Catalytic activity for soot oxidation is carried out on CS*x* samples, and the $T_{50}$ temperature is in between 480–540 °C. Fluorite phase samples (CS10 CS30) showed higher surface area, lower degree of agglomeration, lower band gap energy, higher oxygen vacancy concentration and better catalytic activity for soot oxidation. Among all the CS*x* samples, CS10 sample displayed highest surface area (38 $m^2/g$), lowest degree of agglomeration (0.36), lowest band gap energy (3.04 eV), highest oxygen vacancy concentration (64%) and highest soot oxidation activity ($T_{50}$ = 480 °C). The order of the soot oxidation activity of CS*x* samples followed the same trend of band gap energy values.

## 1. Introduction

Application of catalysts predominantly in soot oxidation reaction manifests the ability to exchange oxygen during the reaction by improved rate of lattice oxygen interaction with soot owing to active oxygen participation. However, poor oxygen diffusion in the un-catalysed reaction is mainly because of the absence of intermediate steps since gaseous oxygen is directly reacted with soot [1]. Nano-size ranged particle demonstrates enhanced activity by increasing defect density and thus promoting active sites for catalytic reactions [2]. Ceria ($CeO_2$) is a promising catalyst attributable to its facile $Ce^{4+/3+}$ redox cycles along with high oxygen storage/release capacity (OSC). Even with a minor addition of dopant to $CeO_2$ the catalytic activity of the material advances substantially [2]. Suitable addition of trivalent dopant into $CeO_2$ host lattice enriches oxygen vacancy as far as a solid solution is established [3]. The fluorite type open arrangement is highly adequate even with the dopant insertion without any structural deformation [4]. Toleration of fluorite structure is high as far as the ionic size of both rare earth dopant ($RE^{3+}$) and $CeO_2$ ($Ce^{4+}$) are of the same range. Beyond the solubility limit, microdomains of cubic phase start growing within fluorite (F) matrix, which results in the hybrid structure [5]. Sm doping on $CeO_2$ lattice leads to mixed metal oxides with the difference in oxidation state and similarity in ionic radius and electronegativity between $Ce^{4+}$ and $Sm^{3+}$. Subsequently, structural stability of host ion is enhanced with the creation of oxygen vacancy by charge compensation mechanism. Some of the applications of Ce-Sm metal oxides are-SOFC [6], CO oxidation [2], luminescence [7], oxygen sensors [8], benzyl alcohol oxidation [9], cyclohexane oxidation [10], light emitting diodes [11] etc.

Both stoichiometry and surface structure are vital issues in the catalytic activity of mixed metal oxides. In a system of $Ce_{1-x}Sm_xO_{2-\delta}$, Artini et al. [6] and Vimal et al. [7] studied the structural variation over whole composition range and found that the phase boundary of F and C exist at $x = 0.3$ [6] and $x = 0.2$ [7], respectively. With the variation in

* Corresponding author.
** Corresponding author at: Energy Materials Research Center, Korea Institute of Science and Technology, Seoul, 136-791 South Korea.
*E-mail addresses:* energyhari@nitk.edu.in (H.P. Dasari), jongho@kist.re.kr (J.-H. Lee).

https://doi.org/10.1016/j.mcat.2018.01.033
Received 5 September 2017; Received in revised form 23 January 2018; Accepted 24 January 2018
Available online 07 May 2018
2468-8231/ 

the region of stable phase formation, oxygen vacancy also deviates since the condition of minimum energy diverges [5,6]. Since surface oxygen formation has a direct correlation with catalytic activity and even oxygen storage capacity of the material is enhanced with the higher availability of surface oxygen, detailed research on this aspect is necessary [12].

Variability in optical properties of rare earth metal oxides doped in host lattice has substantial influence in defect concentration, lattice strain and crystal symmetry [7]. The band gap energy of mixed metal oxides directly corresponds to excitation energy ligand to metal in an oxide. Band gap energy as a critical descriptor for catalytic activity in propene oxidation was studied using mixed metal oxides by Getsoian et al. [13], but the validity of their conclusion upon other ceria-based materials in catalytic activity is not yet extensively executed [13]. Also, the property that is key to enhance the catalytic activity of Ce-Sm metal oxide is not however solely discussed in detail.

This work emphasises the synthesis of binary metal oxide over a whole composition range of $CeO_2$-$Sm_2O_3$ using the EDTA-Citrate method. The synthesised samples were analysed using different characterisation techniques to find the structural property variation with dopant addition. The samples were tested for soot oxidation and the correlation of activity with different structural parameters was further analysed and discussed in depth.

## 2. Experimental details

### 2.1. Materials synthesis

Nano-crystalline binary metal oxide samples of $CeO_2$-$Sm_2O_3$ at varying composition were synthesised using the EDTA-Citrate method [15]. AR grade chemicals were used for the synthesis. Cerium nitrate hexahydrate and Samarium nitrate hexahydrate were used to synthesise the binary mixed metal oxides. Ammonium hydroxide solution was used to adjust the pH. The chelating agents used for this synthesis were Citric acid monohydrate and Ethylene Diamine Tetra Acetic acid (EDTA). Stoichiometric ratios of metal nitrates were added in such a way that the composition of $Sm_2O_3$ on $CeO_2$ varies from 0 to 100%. Synthesis procedure of EDTA-Citrate complexing method [14] was followed, and the black precursor solid obtained was oven dried at 150 °C/24 h followed by heat treatment at 350 °C/12 h. Further calcination at 600 °C/5 h was carried to get the corresponding metal oxide samples. The obtained metal oxides, $Ce_xSm_{1-x}O_{2-\delta}$ (where $x$ = 0-1) was represented as $CeO_2$, CS$x$ ($x$ = 10–90 mol%) and $Sm_2O_3$, respectively.

### 2.2. Materials characterization

Raman spectra of the CS$x$ samples were obtained using Raman spectroscopy (Bruker: RFS 27 Model Raman spectrometer) with a charged-couple device (CCD) detector and a triple polychromator. Nd: YAG laser ($\lambda$ = 1064 nm) was used as an excitation source with a laser power of 10 mW on the sample point. The CS$x$ samples were also characterized using X-ray diffraction (XRD), Transmission Electron Microscopy (TEM) and X-Ray Photoemission spectroscopy (XPS) techniques and the instrument details and the operating conditions were same as described in our earlier report by Anatharaman et al. [15]. The surface area of the CS$x$ samples was obtained using Surface area analyser Smart Sorb 92/93 model (Smart Instruments Company) operating on the principle of $N_2$ adsorption based on single point BET method. The sample holder along with the sample was placed in an oven at 150 °C/2 h to remove any moisture present in the sample before the test. Then, the tube was connected to the carrier gas line of the instrument to perform the test. Field Emission-Scanning Electron Microscopy (FE-SEM)/Energy Dispersive Spectroscopy (EDS) (CARL ZEISS SIGMA) was used to obtain the morphology and the composition of the CS$x$ samples. UV–vis NIR spectrometer (Cary 5000) was used to obtain the UV–vis Diffusive Reflectance Spectroscopy (DRS) measurements of the CS$x$ samples.

### 2.3. Soot oxidation activity

For soot oxidation activity measurements, standard soot (Printex U), (Orion Engineered Carbons) was used [16], and the experiments were conducted in tight contact condition by mixing it for 30 min with the catalyst in 4:1 ratio in a mortar and pestle. The obtained mixture was preheated at ~100 °C to remove any moisture content present. As described in the earlier reports [3,17], TGA instrument (TG/DTA 6300) was used to obtain the weight loss associated with the soot oxidation reaction [17]. The mixture (catalyst + soot) was kept in the sample holder of TGA instrument, and the change in weight was recorded with the increase in temperature (from 200 to 700 °C) with a heating rate of 10 °C/min in the presence of air at a flow rate of 100 ml/min [17]. The reproducibility for the soot oxidation activity of each sample was performed to validate the results and the order of the catalytic activity.

## 3. Results and discussion

### 3.1. XRD analysis

Fig. 1(a) depicts the XRD patterns of CS$x$ sample calcined at 600 °C/

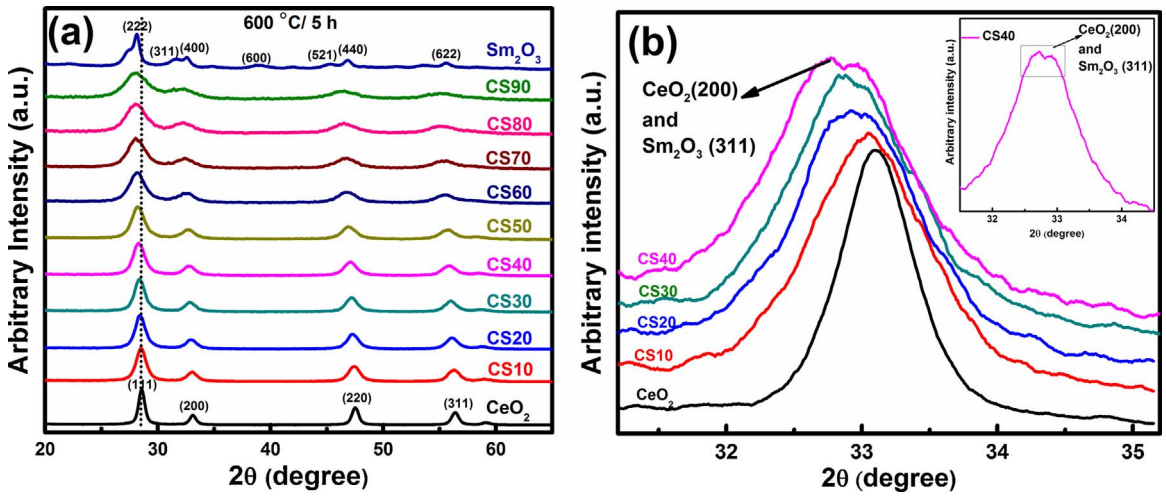


**Fig. 1.** (a) XRD pattern of CS$x$ samples calcined at 600 °C/5 h (b) XRD pattern corresponding to (111) peaks up to CS40 and peak splitting for CS40 sample (inset).

**Table 1**
Crystallographic data, BET surface area, particle size, lattice strain and degree of agglomeration of CS*x* metal oxides calcined at 600 °C/5 h.

| Metal oxide | Crystallite size[a] (nm) | Lattice constant[b] (Å) | | BET Surface area ($m^2$/g) | Particle size[c] (nm) | Lattice strain[d] (ε) | Degree of agglomeration[e] (ϕ) |
|---|---|---|---|---|---|---|---|
| | | (111) | (222) | | | | |
| $CeO_2$ | 13.1 | 5.40 | – | 24 | 36 | 0.011 | 0.36 |
| CS10 | 08.2 | 5.42 | 10.83 | 38 | 23 | 0.018 | 0.36 |
| CS20 | 08.0 | 5.43 | 10.86 | 45 | 19 | 0.018 | 0.42 |
| CS30 | 07.9 | 5.44 | 10.88 | 35 | 24 | 0.018 | 0.32 |
| CS40 | 06.9 | 5.45 | 10.91 | 29 | 29 | 0.021 | 0.23 |
| CS50 | 06.7 | 5.47 | 10.93 | 24 | 35 | 0.022 | 0.19 |
| CS60 | 05.6 | 5.48 | 10.97 | 18 | 46 | 0.026 | 0.12 |
| CS70 | 05.1 | 5.49 | 10.99 | 16 | 50 | 0.029 | 0.10 |
| CS80 | 04.6 | 5.51 | 11.01 | 14 | 58 | 0.032 | 0.08 |
| CS90 | 04.4 | 5.51 | 11.02 | 10 | 77 | 0.033 | 0.06 |
| $Sm_2O_3$ | 07.2 | – | 11.07 | 08 | 95 | 0.019 | 0.07 |

[a] Crystallite size using Scherrer equation from XRD = $\frac{n\lambda}{\beta \cos \theta}$.
[b] Lattice constant for cubic phase from XRD = $d\sqrt{h^2 + k^2 + l^2}$.
[c] Particle size calculated using BET surface area = $\frac{6000}{\rho \times SA_{BET}}$.
[d] Lattice strain from XRD = $\frac{\beta}{4 \tan \theta}$.
[e] Degree of agglomeration from XRD (ϕ) = $\frac{Crystallite\ size\ from\ XRD}{Particle\ size\ from\ BET\ Surface\ area}$.

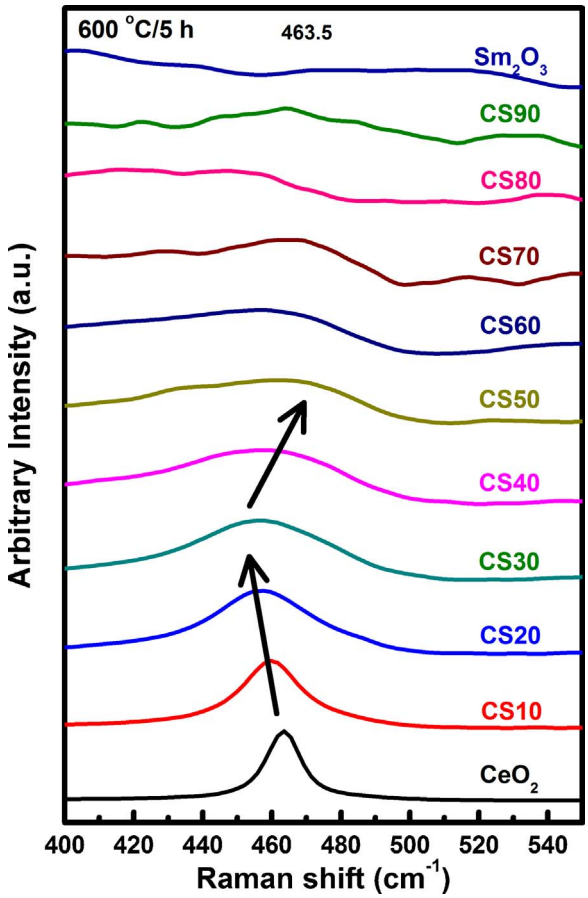


**Fig. 2.** Raman spectra of CS*x* samples calcined at 600 °C/5 h.

5 h. $CeO_2$ and $Sm_2O_3$ samples displayed mainly pure fluorite and cubic structures, respectively [18,19]. From Fig. 1(a) up to CS90 sample, most of the peaks resemble $CeO_2$ peaks [20]. A slight shift in (111) peak of $CeO_2$ towards lower angle is definite in Fig. 1(a) with the dopant addition and this confirms a lattice expansion due to the substitution of larger ionic radii $Sm^{3+}$ (1.086 Å) [21] compared to $Ce^{4+}$ (1.012 Å) [21]. On clear observation of specific peak range, as shown in Fig. 1(b), a distinct peak splitting for (200) plane of $CeO_2$ and (311) plane of $Sm_2O_3$ significantly from CS40 sample onwards is seen [20]. Thus, it is evident that up to CS30, samples are in single fluorite phase and from CS40 to CS90 samples exists in bi (fluorite + cubic) phase. From the literature [5–7,22], the extent of solubility (presence of single or bi-phase) of the ceria-based samples is affected by various parameters like synthesis method, calcination temperature and reduction/oxidation atmosphere. From Fig. 1(a) & (b), CS*x* samples prepared obtained by the current synthesis method, exists in three phases (CS10 CS30 (fluorite phase), CS40–CS90 (bi (fluorite + cubic) phase) and $Sm_2O_3$ (cubic phase)) depending on the dopant content.

Table 1 tabulates the calculated values of crystallographic data, BET surface area, particle size, the degree of agglomeration and lattice strain. The crystallite size (D) of the CS*x* samples is in the range of 05–13 nm. With the increase in Sm content, a decrease in crystallite size, an increase in lattice constant and lattice strain is noticed. This can be due to resistance to crystal growth by Ce-O-Sm bond formation [2], reduction in valancy that reduces the electrostatic force [9] and oxygen vacancy creation [23], respectively.

The BET surface area of all CS*x* sample is in the range of 08–45 $m^2$/g (see Table 1). The surface area values of pure $CeO_2$ and $Sm_2O_3$ samples are 24 and 08 $m^2$/g, respectively. Fluorite phase samples (CS10–CS30) displayed higher surface area values than the bi-phasic (CS40–CS90), and cubic phase sample ($Sm_2O_3$) and a similar trend is observed for degree of agglomeration. The surface area value of ceria-based samples obtained by this synthesis method is lower than the surface area of samples prepared by other synthesis methods like co-precipitation [2], deposition-precipitation (calcined at 500 °C) [24], sol-gel (calcined at 500 °C) [25] and hydrothermal [26] methods. This is because, the EDTA-citrate method is a type of solution combustion synthesis, which yields low surface areas due to its exothermic nature, and depends on the calcination temperature to obtain the products. The advantage of the EDTA-citrate method is that the catalyst production rates per batch can be higher and homogeneity at the molecular level is better than the above said synthesis methods [14,27]. Because the particle size is higher than the crystallite size, the calculated degree of agglomeration is also higher. CS*x* samples displayed a higher degree of agglomeration and low BET surface area with the Sm content, and this may deteriorate the catalytic activity [28].

### 3.2. Raman spectroscopy analysis

Fig. 2 represents the Raman spectra of CS*x* samples. Up to CS50 sample, the signature peak (~463 $cm^{-1}$) of $CeO_2$ can be seen with a redshift (lower wavelength), and it can be ascribed to $F_{2g}$ (O-Ce-O) mode of fluorite structure [29]. Apart from the signature peak,

**Table 2**
$I_{Ov}/I_{F2g}$, Composition, Reducibility ratio, $O_\beta/(O_\alpha + O_\beta + O_\gamma)$, Band gap and $T_{50}$ temperature of CS*x* samples calcined at 600 °C/5 h.

| Metal oxide | $I_{Ov}/I_{F2g}$[a] | Composition from EDS (mole%) | | Reducibility ratio[b] (%) | $O_\beta/(O_\alpha + O_\beta + O_\gamma)$ (%) | Band gap[c] (eV) | $T_{50}$[d] (°C) |
|---|---|---|---|---|---|---|---|
| | | Ce | Sm | | | | |
| $CeO_2$ | – | 100.0 | 0.0 | 65 | 24 | 3.10 | 530 |
| CS10 | 0.05 | 93.6 | 6.4 | 25 | 64 | 3.04 | 480 |
| CS20 | 0.12 | 81.6 | 18.4 | 41 | 45 | 3.06 | 500 |
| CS30 | 0.20 | 73.1 | 26.9 | 4 | 34 | 3.07 | 511 |
| CS40 | 0.35 | 62.6 | 37.4 | 25 | 12 | 3.06 | 502 |
| CS50 | 0.51 | 52.7 | 47.3 | 16 | 07 | 3.09 | 512 |
| CS60 | – | 40.2 | 59.8 | – | 08 | 3.10 | 531 |
| CS70 | – | 32.3 | 67.7 | – | 10 | 3.10 | 537 |
| CS80 | – | 21.7 | 78.3 | 35 | 06 | 3.12 | 542 |
| CS90 | – | 11.7 | 88.3 | 05 | 34 | 3.15 | 538 |
| $Sm_2O_3$ | – | 0.0 | 100.0 | – | 54 | 5.06 | 537 |
| Soot | – | – | – | – | – | – | 600 |

[a] Intensity ratio from Raman spectra.
[b] Reducibility ratio from XPS = $\frac{Ce^{3+}}{Ce^{3+} + Ce^{4+}}$.
[c] Direct band gap energy from UV–vis DRS using Tauc's plot.
[d] $T_{50}$ temperature from Soot oxidation activity.

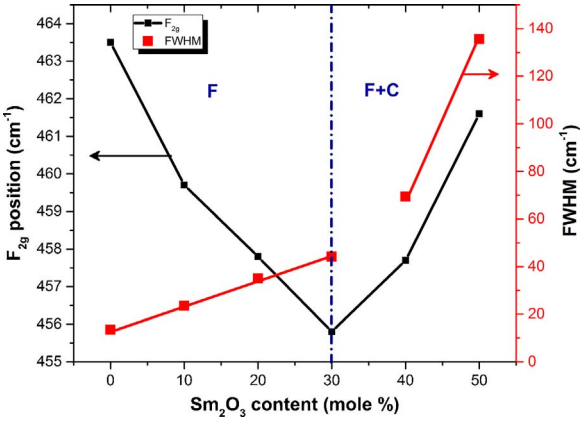


**Fig. 3.** Variation of $F_{2g}$ peak shift and FWHM of $F_{2g}$ peak with $Sm_2O_3$ content of CS*x* samples calcined at 600 °C/5 h.

additional peaks at 560 and 610 $cm^{-1}$ attributed to the formation of oxygen vacancies were noticed in CS20 sample (Fig. S2) [30]. In Table 2, the relative ratio of the oxygen vacancy ($I_{Ov}/I_{F2g}$) of CS*x* samples are given and it shows an increase in the relative ratio with the increase in Sm content up to CS50 sample. Peak shift and FWHM of the $F_{2g}$ peak are plotted with an increase in Sm content and shown in Fig. 3 [5]. For fluorite phase samples (CS10–CS30) $F_{2g}$ peak shifts towards lower frequency and afterwards there is a shift towards a higher value. Similarly, the slope of FWHM is different for samples in fluorite and bi-phase as evident in Fig. 3. This change in position and peak width with the dopant is related to the reduction in Ce content and degree of disorder in excited bond, that confirms the secondary phase formation [5]. The $F_{2g}$ peak is taken only till CS50 since there is no significant Raman peak afterwards. Similar to XRD results, phase separation is also evident from Raman results.

### 3.3. SEM-EDS & TEM analysis

Fig. 4(a–e) depicts the SEM images of CS*x* samples, and with an increase in Sm content, an increase in particle agglomeration is noticed, and this corroborates with the degree of agglomeration obtained using XRD and BET surface area values. Fig. 4(f) shows the EDS analysis of CS10 sample where the presence of Ce, Sm and O elements are noticed. Similarly, the CS*x* sample composition is confirmed using EDS analysis and shown in Table 2. TEM, HR-TEM and SAED patterns of CS10 sample is shown in Fig. 5. Fig. 5(a) shows crystalline spherical particles in the nanometer size range. Fig. 5(b) highlights the fringes of particles with d-spacing corresponding to (111) and few (200) planes. Fig. 5(c) with SAED pattern of diffraction rings indexed to fluorite $CeO_2$ plane is similar to XRD results.

### 3.4. XPS analysis

Fig. 6(a) illustrates the Ce 3d core-level spectrum of selected samples of $CeO_2$, CS10, CS30, CS50, CS70 and CS90. The spin-orbital multiplets corresponding to Ce $3d_{5/2}$ and $3d_{3/2}$ confirms the multi oxidation state of $CeO_2$ in $Ce^{4+}$ (v and u‴) and $Ce^{3+}$ ($v_0$, v′ and $u_0$) respectively [29]. The reducibility ratio of the samples is calculated and tabulated in Table 2 for comparison purpose [10]. Peak at ~1080–1085 eV in Sm $3d_{5/2}$ spectrum of CS30, CS50, CS70, CS80 and $Sm_2O_3$ displayed in Fig. 6(b) confirms the presence of $Sm^{3+}$ in all the samples [18] and Fig. 6(c) depicts the O 1s XPS spectrum of specific $CeO_2$, CS10, CS50, CS70, CS90 and $Sm_2O_3$ samples. The O 1s spectra confirm three different oxygen species present in all the samples that correspond to lattice oxygen ($O_\alpha$), surface oxygen vacancy ($O_\beta$) and carbonate, hydroxyls and chemisorbed water ($O_\gamma$) [28]. The relative percentage of surface oxygen is given in Table 2. CS*x* samples in fluorite (F) phase are having the highest surface oxygen vacancy and $Ce^{3+}$ concentration that may enhance the catalytic activity when compared to the samples in bi-phasic (F + C) and cubic (C) phase.

### 3.5. UV–vis DRS analysis

UV–vis DRS of CS*x* samples calcined at 600 °C/5 h is shown in Fig. 7(a). $CeO_2$ sample exhibits two absorption maxima centred at 274 nm and 347 nm which is assigned to O 2p and Ce 4f state charge transfer and inter-band transitions, respectively [29]. These peaks are consistent in most of the samples. The absorption peaks centred at 371, 407 and 473 nm for $Sm_2O_3$ is designated to f-f electronic transitions, and 315 nm may result from the $O^{2-} \rightarrow Sm^{3+}$ charge transfer band [31,32]. Traces of Sm is significant from CS50 onwards with a minor peak at ~470 nm that confirms the bi-phase formation as observed from XRD patterns and Raman spectra of the CS*x* samples.

The Tauc's plot [33] obtained from UV–vis DRS data is depicted Fig. 7(b) and the calculated direct band gap energy values (3.0 eV–5.1 eV) are given in Table 2, the value (for $CeO_2$ and $Sm_2O_3$ samples) matches with the literature [31]. Among all the CS*x* samples, CS10 sample displayed the least band gap energy (3.04 eV) due to a decrease in oxygen vacancy formation energy and this corroborates the results obtained from XPS data where CS10 sample displayed higher oxygen

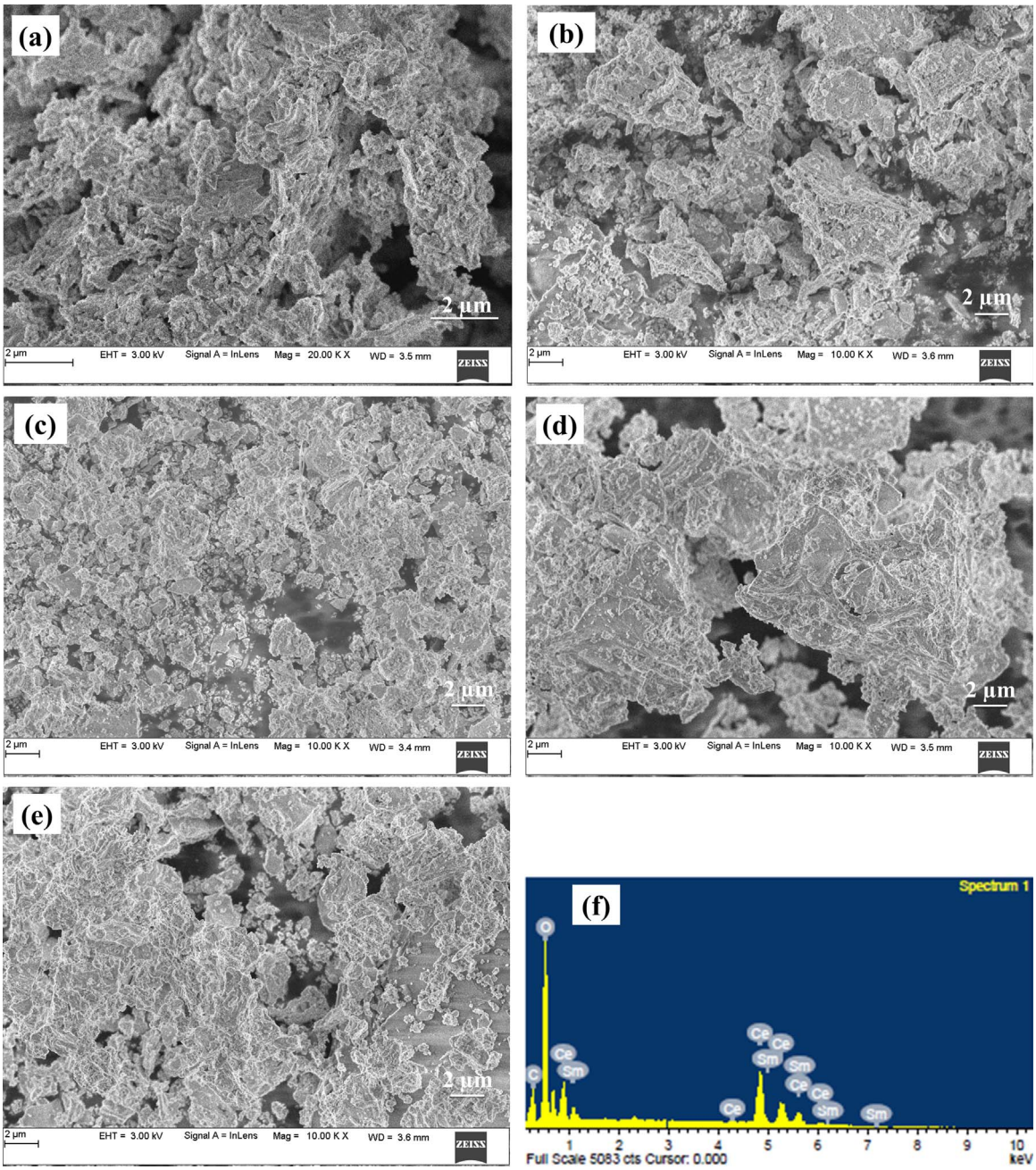


**Fig. 4.** SEM morphology of (a) $CeO_2$; (b) CS10 (c) CS50; (d) CS90 (e) $Sm_2O_3$ and (f) EDS image of CS 10 sample.

vacancy formation [34,35]. Substitution of Sm lowers the band gap energy for fluorite phase samples (CS10–CS30), due to the replacement of Ce 4f by Sm 4f which is comparatively highly filled with higher energy [13]. With the increase in Sm content further for bi-phase (CS40–CS90), secondary phase increases the band gap energy. The results obtained by Gestoian et al. [13] states that the band gap energy is an important descriptor in propene oxidation reaction. It is clear from the XRD, Raman spectroscopy, XPS and UV–vis DRS data that the phase cooperation is influencing the oxygen vacancy formation and band gap energy of the CS*x* samples. Phase cooperation plays a key role in fine-tuning of the descriptors (in this case oxygen vacancy formation and band gap energy) which play a critical role in enhancing the oxidation reactions.

### 3.6. Soot oxidation activity

Soot oxidation reaction carried out under tight contact condition using the whole composition of CS*x* samples as catalyst are illustrated in Fig. 8(a) as a function of temperature in the range of 200–700 °C. The variation in activity with an increase in dopant concentration are compared using $T_{50}$ value (See Fig. 8(b)), and the values are specified in Table 2. $CeO_2$ has a $T_{50}$ temperature of 530 °C due to its strong redox properties. The increasing order of $T_{50}$ value is: CS10 < CS20–CS40 < CS30–CS50 < CS80 < $CeO_2$ < CS60 < CS70–$Sm_2O_3$–CS90. It is evident that there is a rapid decrease in temperature with even quite a small quantity of Sm dopant content of 10 mol% from 530 °C to 480 °C for CS10 and $CeO_2$, respectively. Fluorite (F) phase samples displayed lower $T_{50}$ temperature than compared to the CS*x* samples in bi-phase (F + C) and cubic (C) phase. Maximum activity is attained for CS10 compared to all other samples.

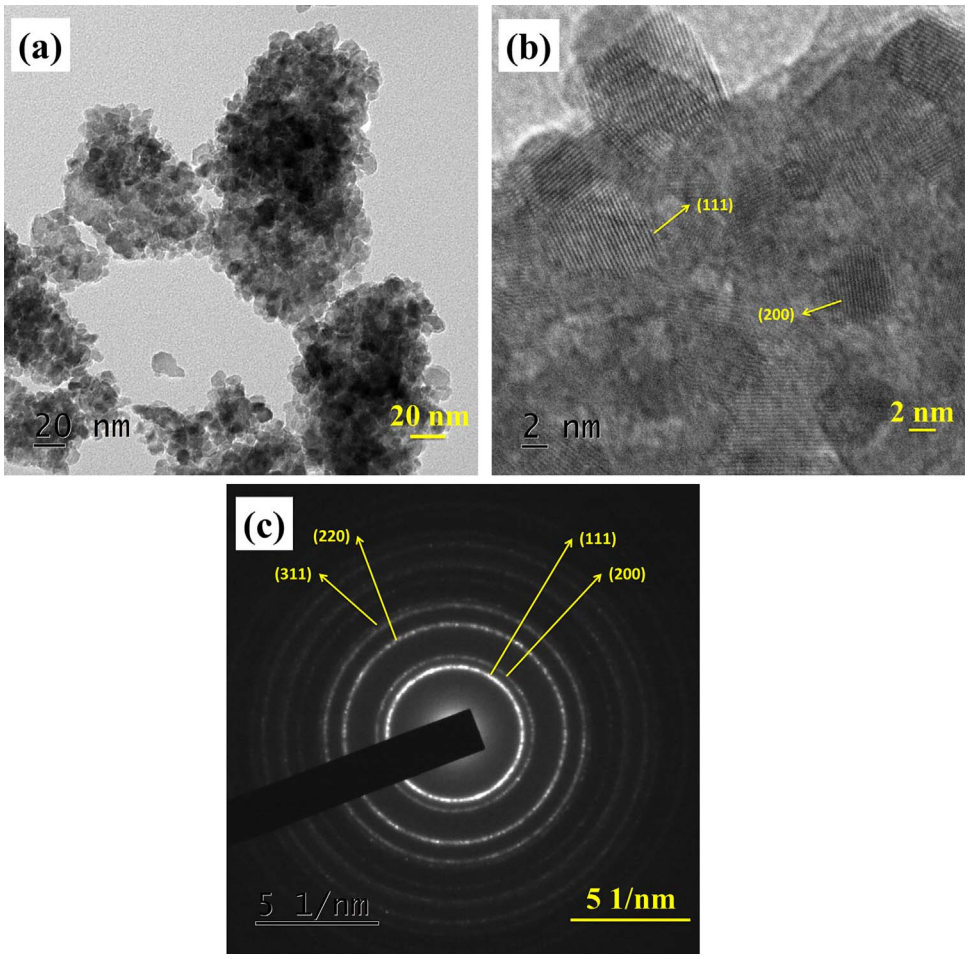


**Fig. 5.** (a) TEM image of CS10 sample; (b) HR-TEM image of CS10 and (c) SAED image of CS10 sample.

Table 3 shows the summarized information that is obtained from various characterization tool and soot oxidation activity. Based on the results obtained from XRD, Raman spectroscopy and UV–vis DRS measurements the CS*x* samples (See Table 3) can be classified into three different segments, that is, fluorite (F), bi-phasic (F + C) and cubic (C) phase. The band gap energy calculated using Tauc's plot from UV–vis DRS follows the same trend as that of soot oxidation activity (see Fig. 8(b)), despite the existence of single and bi-phasic regions. The CS*x* samples in fluorite (F) phase displayed high surface area, a low degree of agglomeration, low band gap energy and high oxygen vacancies than compared to the CS*x* samples in bi-phasic (F + C) and cubic (C) phase and these lead to a higher catalytic activity of the samples. Thus, it can be inferred that the activity is phase dependent. For oxidation processes, Grasselli et al. [36], postulated seven pillars (phase cooperation,

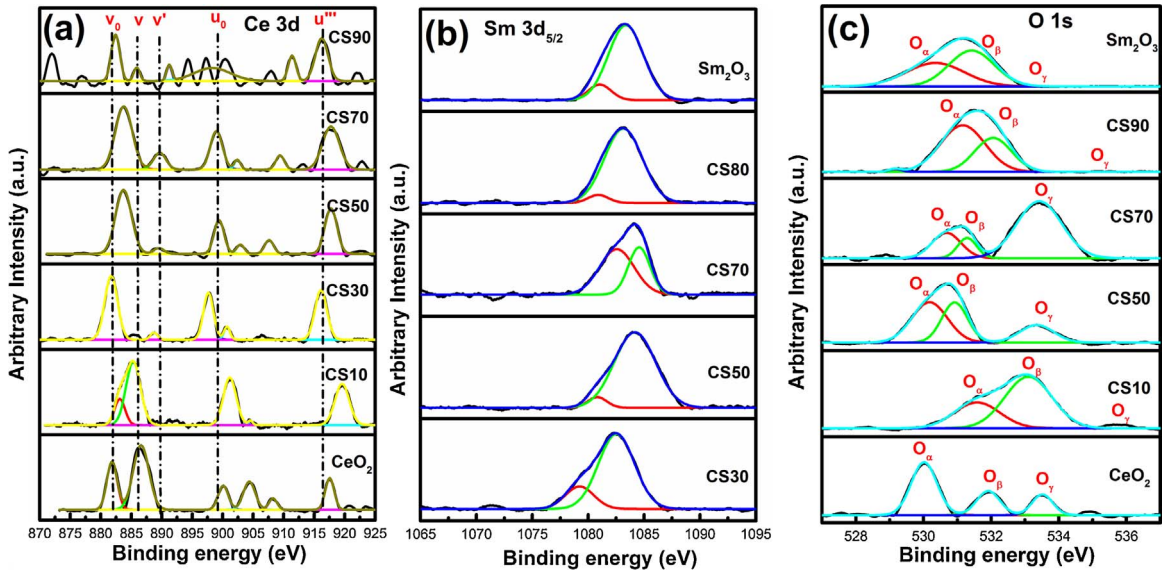


**Fig. 6.** XPS peaks of (a) Ce 3d of specific samples; (b) Sm 3d of specific samples and (c) O 1s of specific samples.

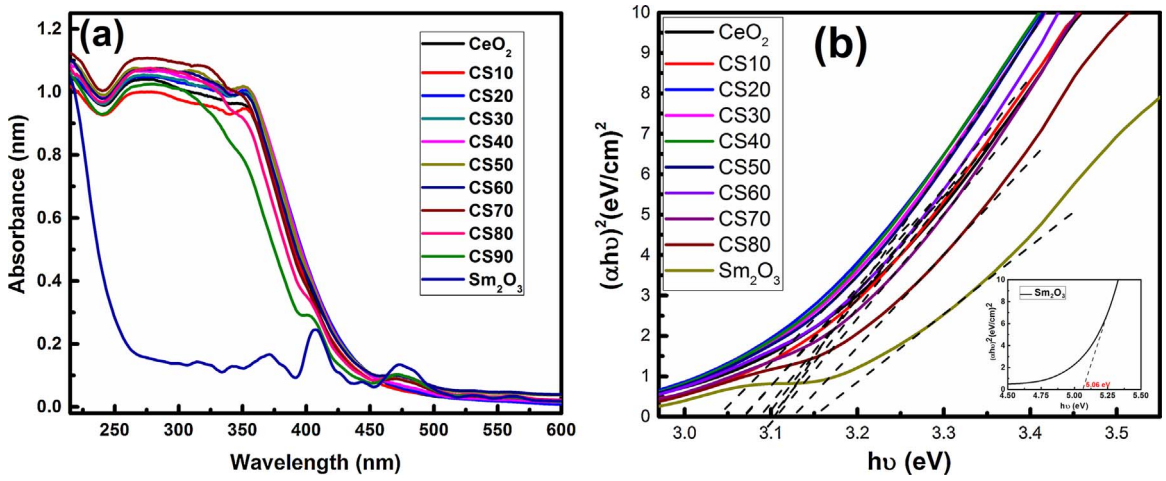


**Fig. 7.** (a) UV–vis DRS of CS*x* samples calcined at 600 °C/5 h (b) Tauc's plot of CS samples obtained from UV–vis DRS plot.

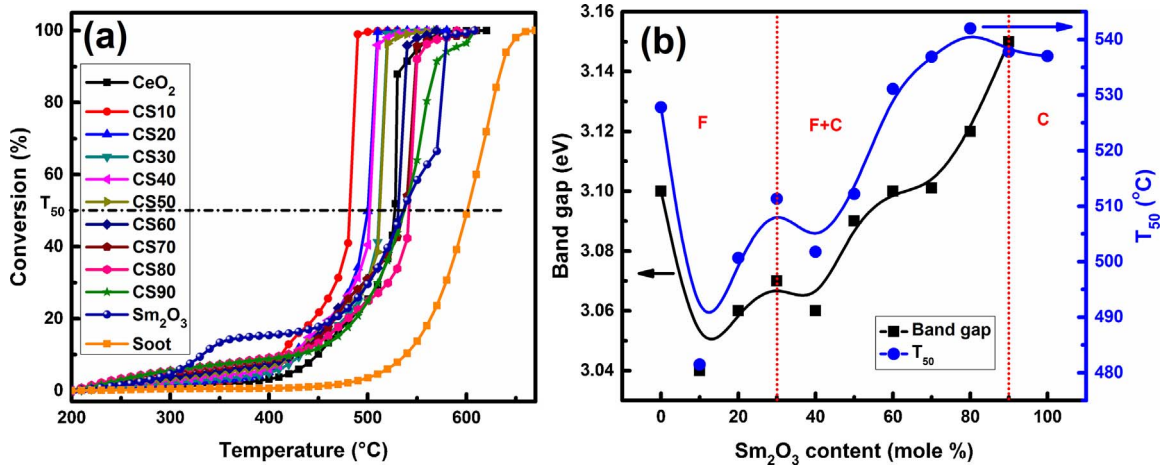


**Fig. 8.** (a) Soot conversion profile of CS*x* samples as catalyst under tight contact (b) Variation in $T_{50}$ and band gap with change in composition.

**Table 3**
Summary of phase of formation, BET Surface area, degree of agglomeration, band gap energy $O_\beta/(O_\alpha + O_\beta + O_\gamma)$ and $T_{50}$ temperature of different sample regions obtained from different characterization tools.

| Metal oxide | Phase of formation[a] | BET Surface area[b] ($m^2$/g) | Degree of agglomeration[c] (%) | Band gap energy[d] (eV) | $O_\beta/(O_\alpha + O_\beta + O_\gamma)$[e] (%) | $T_{50}$[f] (°C) |
|---|---|---|---|---|---|---|
| $CeO_2$ | Pure Fluorite (F) | 24 | 0.36 | 3.10 | 24 | 530 |
| CS10–CS30 | Fluorite (F) | 35–45 | 0.32–0.42 | 3.04–3.07 | 34–65 | 480–510 |
| CS40–CS90 | Bi-Phasic (F + C) | 10–29 | 0.06–0.23 | 3.06–3.15 | 5–34 | 500–540 |
| $Sm_2O_3$ | Pure Cubic (C) | 08 | 0.07 | 5.06 | 54 | 537 |

[a] Obtained from XRD, Raman spectroscopy and UV–vis DRS.
[b] Obtained from BET surface area analyser.
[c] Calculated as the ratio of crystallite size and particle size obtained from BET surface area.
[d] Obtained using Tauc's plot from UV–vis DRS.
[e] Obtained from O1s XPS peaks.
[f] Obtained from Soot oxidation analysis using CSx samples as catalyst.

redox, metal-oxygen bond, lattice oxygen, host structure, multi-functionality of active sites, and site isolation) to describe the activity and selectivity of the catalysts. Even though these pillars provides conventional guidelines, they are described qualitatively and difficult to be mapped directly to a particular fingerprint during conducting experiments. Therefore, this list gives a general principle, rather than quantitative parameter that can be adjusted to reach the desired activity. From the present study, phase cooperation is playing a significant role in controlling the properties like surface area, degree of agglomeration, band gap energy and oxygen vacancies, which have a direct effect on soot oxidation activity.

In the presence of $CeO_2$ based catalyst, soot is oxidised by the active oxygen formed in the intermediate step from the catalyst surface and forms $CO/CO_2$ as per MvK mechanism. For soot oxidation to take place, more than the surface contact points, active centres (oxygen defects) for enhancing the reaction plays a critical role. However, it is not a single parameter such as contact point that decides the soot oxidation activity of the current sample, but a combination of different structural parameters dictates the soot oxidation activity of $CeO_2$-$Sm_2O_3$ samples [37].

## 4. Conclusion

The EDTA-citrate complex method was adopted to synthesise $CeO_2$, CS*x* (*x* = 10–90) and $Sm_2O_3$ metal oxide samples. From XRD, Raman analysis and UV–vis DRS analysis of CS*x*, samples exists in three phases: (CS10–CS30 (fluorite phase), CS40–CS90 (bi (fluorite + cubic) phase) and $Sm_2O_3$ (cubic phase)) depending on the dopant content. The CS*x* samples in fluorite (F) phase displayed high surface area, low degree of agglomeration, low band gap energy and high oxygen vacancies than compared to the CS*x* samples in bi-phasic (F + C) and cubic (C) phase. Among the CS*x* samples, CS10 sample displayed high surface area (38 $m^2$/g), a low degree of agglomeration ($\phi$ = 0.36), low band gap energy (3.04 eV) and high oxygen vacancy concentration (64.4%). This factors resulted in enhancing its soot oxidation activity ($T_{50}$ = 480 °C).

## Authors contribution

APA and GJ obtained all the experimental data. MRP contributed to material synthesis. XRD and BET surface area data were provided UBB and HD, respectively. The study was conceived by HPD. APA, GJ, HPD and JHL has contributed in analysing the experimental data, writing and editing the document.

## Acknowledgements

KIST-IRDA Alumni Project 2017 (2Z05100-17-083) has funded this work. We acknowledge MRC, MNIT Jaipur for facilitating Raman Spectroscopy and XPS data. Also, thank SAIF STIC, Cochin for UV–vis DRS and TEM data and Mangalore University for SEM-EDS data.

## Appendix A. Supplementary data

Supplementary data associated with this article can be found, in the online version, at http://dx.doi.org/10.1016/j.mcat.2018.01.033.

## References

[1] A. Bueno-López, K. Krishna, M. Makkee, J.A. Moulijn, Catal. Lett. 99 (2005) 203–205.
[2] K. Kuntaiah, P. Sudarsanam, B.M. Reddy, A. Vinu, RSC Adv. 3 (2013) 7953.
[3] T. Vinodkumar, B.G. Rao, B.M. Reddy, Catal. Today 253 (2015) 57–64.
[4] G.R. Rao, B.G. Mishra, Bull. Catal. Soc. India 2 (2003) 122–134.
[5] C. Artini, M. Pani, M.M. Carnasciali, J.R. Plaisier, G.A. Costa, Inorg. Chem. 55 (2016) 10567–10579.
[6] C. Artini, M. Pani, M.M. Carnasciali, M.T. Buscaglia, J.R. Plaisier, G.A. Costa, Inorg. Chem. 54 (2015) 4126–4137.
[7] G. Vimal, K.P. Mani, P.R. Biju, C. Joseph, N.V. Unnikrishnan, M.A. Ittyachen, Acta Metall. Sin. 28 (2015) 758–765.
[8] S. Gupta, S.V.N.T. Kuchibhatla, M.H. Engelhard, V. Shutthanandan, P. Nachimuthu, W. Jiang, L.V. Saraf, S. Thevuthasan, S. Prasad, Sens. Actuators B Chem. 139 (2009) 380–386.
[9] S. Mandal, K.K. Bando, C. Santra, S. Maity, O.O. James, D. Mehta, B. Chowdhury, Appl. Catal. A Gen. 452 (2013) 94–104.
[10] N. Sutradhar, A. Sinhamahapatra, S. Pahari, M. Jayachandran, B. Subramanian, H.C. Bajaj, A.B. Panda, J. Phys. Chem. C 115 (2011) 7628–7637.
[11] S. Kaur, P. Kaur, G.P. Singh, D. Arora, S. Kumar, D.P. Singh, J. Lumin. 180 (2016) 190–197.
[12] C. Sun, D. Xue, Phys. Chem. Chem. Phys. 15 (2013) 14414–14419.
[13] A.B. Getsoian, Z. Zhai, A.T. Bell, J. Am. Chem. Soc. 136 (2014) 13684–13697.
[14] D.H. Prasad, S.Y. Park, E.O. Oh, H. Ji, H.R. Kim, K.J. Yoon, J.W. Son, J.H. Lee, Appl. Catal. A Gen. 447–448 (2012) 100–106.
[15] A.P. Anantharaman, H.P. Dasari, J.-H. Lee, H. Dasari, G.U.B. Babu, Catal. Lett. 147 (2017) 1–13.
[16] C.J. Tighe, M.V. Twigg, A.N. Hayhurst, J.S. Dennis, Carbon N. Y. 107 (2016) 20–35.
[17] K. Krishna, A. Bueno-López, M. Makkee, J.A. Moulijn, Appl. Catal. B Environ. 75 (2007) 189–200.
[18] P. Sudarsanam, K. Kuntaiah, B.M. Reddy, New J. Chem. 38 (2014) 5991–6001.
[19] X.L. Sun, A.I.Y. Tok, R. Huebner, F.Y.C. Boey, J. Eur. Ceram. Soc. 27 (2007) 125–130.
[20] S.-F. Wang, C.-T. Yeh, Y.-R. Wang, Y.-C. Wu, J. Mater. Res. Technol. 2 (2013) 141–148.
[21] D.C. Ghosh, R. Biswas, Int. J. Mol. Sci. 4 (2003) 379–407.
[22] D.H. Prasad, H. Ji, H. Kim, J. Son, B. Kim, H. Lee, J. Lee, Appl. Catal. B Environ. 101 (2011) 531–539.
[23] C. Peng, Y. Wang, K. Jiang, B.Q. Bin, H.W. Liang, J. Feng, J. Meng, J. Alloys Compd. 349 (2003) 273–278.
[24] D.N. Durgasri, T. Vinodkumar, F. Lin, I. Alxneit, B.M. Reddy, Appl. Surf. Sci. 314 (2014) 592–598.
[25] Q. Liang, X. Wu, D. Weng, H. Xu, Catal. Today 139 (2008) 113–118.
[26] M. Lykaki, E. Pachatouridou, E. Iliopoulou, S.A.C. Carabineiro, M. Konsolakis, RSC Adv. 7 (2017) 6160–6169.
[27] D. Sanjay Kumar, K. Ananthasivan, S. Amirthapandian, A. Dasgupta, G. Jogeswara Rao, J. Nucl. Mater. 497 (2017) 16–29.
[28] W. Zhang, X. Niu, L. Chen, F. Yuan, Y. Zhu, Sci. Rep. 6 (2016) 1–10.
[29] D.H. Prasad, S.Y. Park, H.I. Ji, H.R. Kim, J.W. Son, B.K. Kim, H.W. Lee, J.H. Lee, J. Phys. Chem. C 116 (2012) 3467–3476.
[30] A. Filtschew, K. Hofmann, C. Hess, J. Phys. Chem. C 120 (2016) 6694–6703.
[31] P. Sathishkumar, R.V. Mangalaraja, T. Pandiyarajan, M.A. Gracia-Pinilla, N. Escalona, C. Herrera, R. Garcia, RSC Adv. 5 (2015) 22578–22586.
[32] B. Padlyak, W. Ryba-Romanowski, R. Lisiecki, V. Adamiv, Y. Burak, I. Teslyuk, A. Banaszak-Piechowska, Opt. Appl. 40 (2010) 427–438.
[33] J. Tauc, R. Grigorovici, A. Vancu, Phys. Status Solidi 15 (1966) 627–637.
[34] S. Kumar, A.K. Ojha, RSC Adv. 6 (2016) 8651–8660.
[35] S.A. Ansari, M.M. Khan, M.O. Ansari, S. Kalathil, J. Lee, M.H. Cho, RSC Adv. 4 (2014) 16782–16791.
[36] R.K. Grasselli, Top. Catal. 21 (2002) 79–88.
[37] M. Capdevila-Cortada, G. Vile, D. Teschner, J. Perez-Ramirez, N. Lopez, Appl. Catal. B Environ. 197 (2016) 299–312.